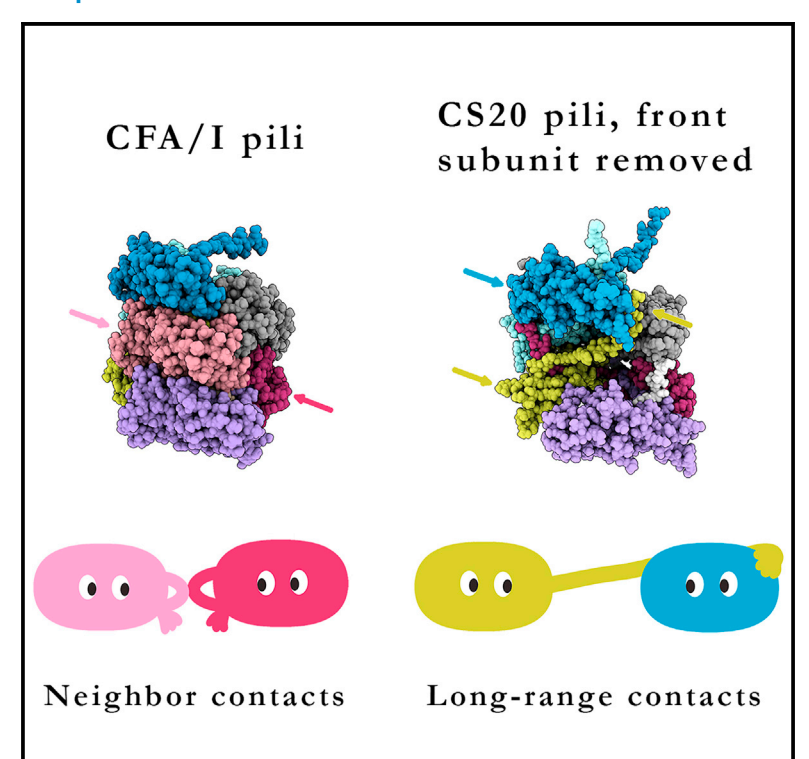
Three structural solutions for bacterial adhesion pilus stability and superelasticity

Graphical abstract



Authors

Matthew H. Doran, Joseph L. Baker, Tobias Dahlberg, Magnus Andersson, Esther Bullitt

Correspondence

bullitt@bu.edu

In brief

Many bacteria initiate disease after sustained binding by specialized filaments. These pili unwind and rewind to decrease the force at the point of cell contact. As demonstrated in Doran et al. pili depend primarily on their structure, rather than on the pilus proteins' genetic code, for the unwinding force.

Highlights

- Pathogenic bacteria bind to human cells via long thin surface filaments called pili
- Genetic similarity is not well correlated with the force needed to unwind pili
- Near-neighbor and long-distance contacts provide the strength of interaction



Structure



Article

Three structural solutions for bacterial adhesion pilus stability and superelasticity

Matthew H. Doran, 1,5 Joseph L. Baker, 2 Tobias Dahlberg, 3 Magnus Andersson, 3,4 and Esther Bullitt 1,6,*

- ¹Department of Physiology & Biophysics, Boston University Chobanian & Avedisian School of Medicine, Boston, MA 02118, USA
- ²Department of Chemistry, The College of New Jersey, Ewing, NJ 08628, USA
- ³Department of Physics, Umeå University, Umeå, Sweden
- ⁴Umeå Centre for Microbial Research (UCMR), Umeå University, Umeå, Sweden
- ⁵Present address: Department of Biological Chemistry & Molecular Pharmacology, Harvard Medical School, Boston MA, USA

⁶Lead contact

*Correspondence: bullitt@bu.edu https://doi.org/10.1016/j.str.2023.03.005

SUMMARY

Bacterial adhesion pili are key virulence factors that mediate host-pathogen interactions in diverse epithelial environments. Deploying a multimodal approach, we probed the structural basis underpinning the biophysical properties of pili originating from enterotoxigenic (ETEC) and uropathogenic bacteria. Using cryo-electron microscopy we solved the structures of three vaccine target pili from ETEC bacteria, CFA/I, CS17, and CS20. Pairing these and previous pilus structures with force spectroscopy and steered molecular dynamics simulations, we find a strong correlation between subunit-subunit interaction energies and the force required for pilus unwinding, irrespective of genetic similarity. Pili integrate three structural solutions for stabilizing their assemblies: layer-to-layer interactions, N-terminal interactions to distant subunits, and extended loop interactions from adjacent subunits. Tuning of these structural solutions alters the biophysical properties of pili and promotes the superelastic behavior that is essential for sustained bacterial attachment.

INTRODUCTION

The initiation of traveler's diarrhea most often requires the sustained adhesion of bacteria via one or more types of adhesion pili. Common to all these adhesion pili is the IgG-like pilin subunit that assembles a multimer extending from the bacterial surface. The development of vaccines against diarrheal diseases remains a priority of the World Health Organization, with pilin subunits from enterotoxigenic *Escherichia coli* (ETEC) as priority pathogens in this initiative. Where endemic, ETEC can cause malnutrition, leading to stunted growth and cognitive development, as well as increase the probability of irritable bowel syndrome. 2-5 ETEC are also the most common cause of diarrhea in travelers to these countries.

Pili expressed on ETEC share many of their structural properties with adhesion pili found on uropathogenic *E. coli* (UPEC). They are hollow helical rods 7–9 nm in diameter with approximately 3.0–3.3 IgG-like subunits per helical turn and a rise per subunit of 7.5–9 Å. Conversely, their genetic sequences, the subunit-subunit contacts between pilins, and their biophysical properties are highly varied, resulting in pili that function in diverse environments. In addition to the ubiquitous seven β -strands that comprise the major adhesion pilins expressed on bacteria in the gut or urinary tract 6 and the ability of pili to unwind, 7 the first nine N-terminal amino acids of one ETEC pilus structure presented here, CS20 pili, forms a staple. The staple, as is also seen in the UPEC-expressed P pili, 8 provides contacts to distant

subunits and thereby stabilizes the quaternary structure. As a class 1 pilus, the genetic sequence of CS20 pili is expected to be similar to that of P pili and type 1 pili. CS20 does not have significant sequence homology with the other two ETEC pili reported here, CFA/I and CS17 pili, although they share an environmental niche in the gastrointestinal tract.

It is common to find expression of multiple pilus types on a single bacterium in vivo (e.g. 10). Type 1 pili that are known to cause urinary tract infections of the bladder also facilitate diarrheal disease; in the gut, type 1 pili are known to enhance disease by coexpression with the most commonly seen ETEC pilus, CFA/I pili. 11 Thus, isotypes of type 1 pili that share more than 90% identity are expressed on UPEC or ETEC and must, therefore, facilitate sustained adhesion in diverse natural environments. For example, UPEC were significantly attenuated in bladder infection and intestinal colonization of mice when the bacteria expressed mutant type 1 pili in which point mutations weakened the quaternary structure (subunit-subunit interactions), resulting in easier unwinding. 12 Since alteration of the quaternary structure changes biophysical properties such as tensile elasticity and unwinding under force, it is important to assess and understand their implication during attachment. Filament unwinding not only makes pili approximately 6-fold longer, 9 it also improves their attachment to adhesin receptors by modulating the load experienced at the attachment site. 13,14 Changing the modulating properties of pili can thereby affect the optimal function of adhesins, especially when they behave as catch bonds. 15



Table 1. Major pilin sequence identity/similarity								
Pilus	Pilin	Type	Class	Clade	CS17	CS20	P pili	Type 1
CFA/I	CfaB	ETEC	5a	α	52/69%	20/36%	23/33%	19/30%
CS17	CsbA	ETEC	5b	α	_	21/32%	20/35%	21/32%
CS20	CsnA	ETEC	1b	γ	-	-	24/35%	25/38%
P pili	PapA	UPEC	1a	π	_	_	_	33/49%
Type 1	FimA	UPEC	1a	Υ	_	_	_	_
Class 5a ¹⁶ ;	Class 5b ^{16,18} ; C	class 1. ¹⁹						

Thus, a better understanding of the interactions that stabilize pilus structures and thereby give rise to their biophysical properties, can help us to understand pilus adaptations related to the environment.

We describe here the structures of three ETEC pili, CFA/1, CS17, and CS20 that we have determined by cryo-electron microscopy (cryo-EM). To understand the mechanisms of their unwinding and rewinding we measured unwinding and rewinding forces using optical tweezers force spectroscopy, performed steered molecular dynamics (sMD) simulations, and calculated interaction energies and buried surface area calculations of their quarternary interactions. We discuss the progression of bond breaking that occurs during pilus unwinding, including loop and N-terminal staple interactions. Including data from two UPEC pili with known structures, P pili⁸ and type 1 pili (PDB: 6Y7S), we provide a structural basis for biophysical adaptations that facilitate the initiation of disease in different environmental niches.

RESULTS

Genetic comparison

Individual pilus subunits expressed on UPEC and ETEC bacteria have significant genetic sequence variability within and between pilus classes. Despite their basic structural similarity, the major pilin subunit sequences are most commonly used to delineate classes, while the use of the sequences of outer membrane usher proteins, through which pilin subunits exit bacteria, are used to define clades. 16,17 As seen in Table 1, sequence analysis of five pili whose structures are known or reported in this paper shows that there is no more than 52% identity between any two pilus types, even within the same class of pilin. In fact, the pili share an average sequence identity of 26% and a median of 22% identity. Sequence similarity ranges from 30% to 69% and, as expected, correlates with the class of pilin (class 1 vs class 5); aligned sequences are shown in Figure S1. Thus, although the fundamental structure of adhesion pili is consistent, there are significant differences in their genetic sequences as well as variations in their biophysical properties, including higher unwinding forces for pili expressed on UPEC vs ETEC bacteria, as discussed below in the section 'Filament unwinding by force spectroscopy'.

Cryo-EM structures

To see how genetic and structural differences affect the biophysical properties of adhesion pili, we first determined the structures of three ETEC pili. These include the genetically similar CFA/I and CS17 pili and also CS20, which is more closely related to pili expressed on UPEC. As shown in Figures 1 and S2, Video S1 and Table S1, we have determined the structures of the helical filaments of CFA/I (PDB: 8EHR), CS17 (PDB: 8EHS), and CS20 (PDB: 8EHT) pili by cryo-EM to resolutions of 3.2 Å, 3.3 Å, and 3.4 Å, respectively, using the RELION helical processing package.20 The diameters of the assembled filaments are 77 Å for CFA/I and CS17 and 85 Å for CS20 pili. Similar to the currently known structures of adhesion pili, subunits oligomerize by fitting the N-terminal β -strand of subunit *n* into a hydrophobic groove in the preceding (n - 1) subunit via a tongue-in-groove mechanism.²¹ Each of the subunits consists of seven β-strands with variable-sized loops extending from the β-strand core. CFA/I and CS17 (Figures 1A and 1B) share a remarkable structural similarity for proteins having a sequence identity of only 52% (Table 1). For example, after superimposing the two subunits, the root-mean-square deviation (RMSD) of the backbone is calculated to be 1.3 Å; see Table S2 for a comparison of all RMSD values, and Table S3 for subunit-subunit contacts. Additionally, each of the loops extending from the β-strand core is in a very similar position (Figures 2B-2D). As in other pili, there is a tongue-in-groove interaction from the n + 1 subunit (sky blue) to subunit n (blue) and multiple contacts with the n + 3 subunit (pink); both pili are contacted by the N-terminal extension of the n + 4 subunit (yellow); and there are connections to the n + 2 subunit (gray).

Although the CS20 pilin CsnA also has a seven-\(\beta\)-strand architecture, it has a larger molecular weight compared with CFA/I and CS17 (17.5 kDa, cf. 15.1 kDa for CFA/I's CfaB and 15.4 kDa for CS17's CsbA), providing longer loops extending from the core structure (Figures 2B-2D and Video S1). These loops in subunit n of CS20 form interactions with the n + 1 (sky blue), n + 2 (gray), and n + 3 (pink) subunits. In addition to longer extending loops, the N-terminal extension of CS20 extends farther and includes a structural moiety called the staple, which was previously observed in UPEC P pili.8 This motif is referred to as the staple because of its role in increasing the strength of distant subunit-to-subunit interactions. In CS20, the staple amino acids (1-9) make contacts that are not present in either CFA/I or CS17. The nine-residue CS20 staple motif reaches back from the n + 2 (gray) to subunit n (blue) subunit and staple residues from n + 4 (yellow), and n + 5 (wine red) subunits reach back to subunit n, as seen in Figure 2 and Video S1. Specifically, these contacts include the base of the n + 2 staple interacting with the top distal end of subunit n; the majority of the n + 4 staple interacting with the proximal end; and the tip of the n + 5 staple interacting with the bottom of the distal side of subunit n. Conversely, the N-terminal extensions of CFA/I and CS17 do not extend significantly beyond the tongue-in-groove region of the previous subunit.

Article CFA/I pili В CS17 pili staple С CS20 pili

Figure 1. Adhesion pili share the same basic architecture

Structure

(A-C) ETEC adhesion pili are helical filaments with approximately three subunits per turn, and 8- to 9-nm diameters. Representative cryo-EM images of CFA/I pili (A), CS17 pili (B), and CS20 pili (C) are shown for each pilus type (left). Thousands of these images were used to compute three-dimensional helical reconstructions (center). Atomic models were fitted into the maps, with a single subunit shown in the same orientation as the map for each pilus type (top right). Models including three subunits are shown rotated 90° (bottom right). While each pilus includes a β-strand that fits into a hydrophobic groove in the preceding subunit, CS20 pilin subunits also include a staple that extends beyond the groove and contacts pilins four and five subunits away. Scale bar for all micrographs, 50 nm. CFA/I, CS17, CS20 PDB: 8EHR, 8EHS, and 8EHT, respectively.

CellPress



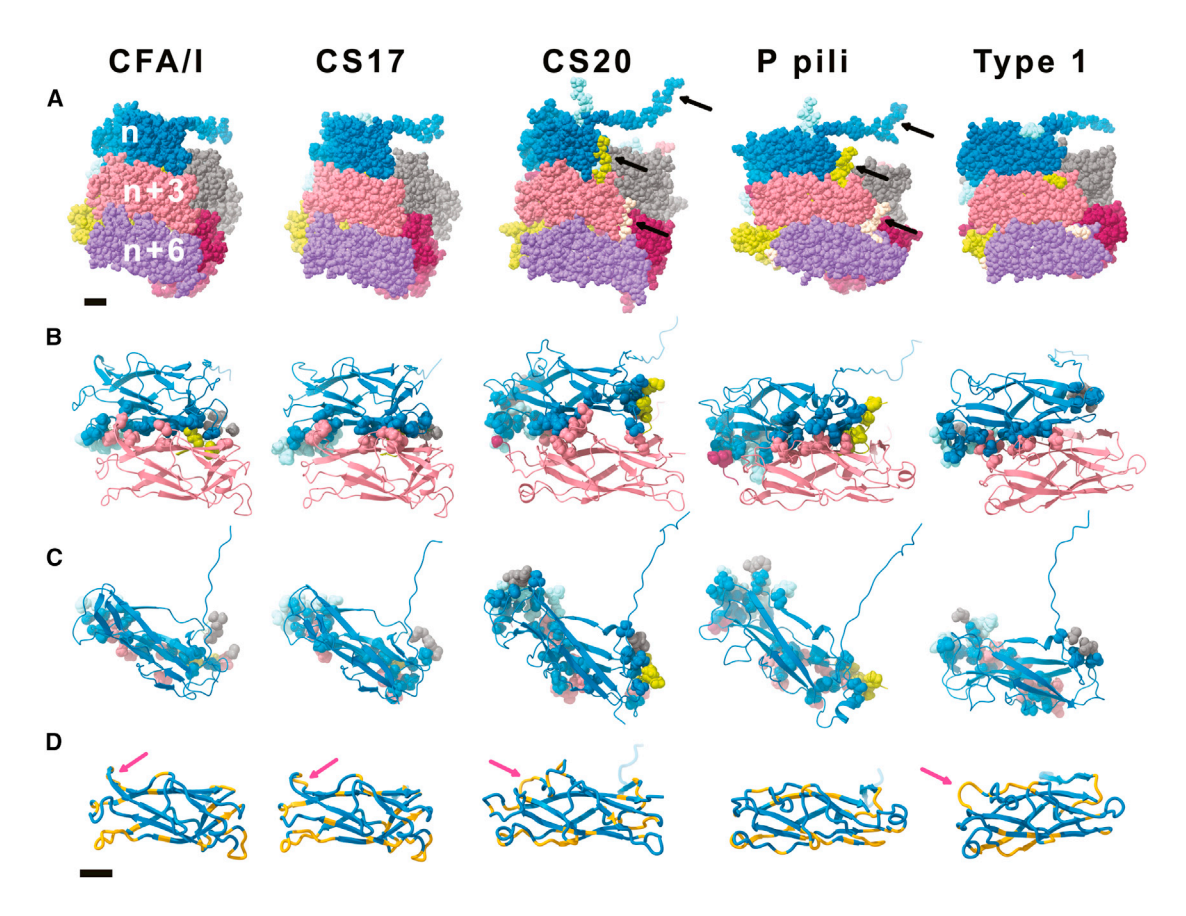


Figure 2. Subunit contacts

(A) Subunit numbering is as in CFA/I. Subunits are individually colored: n (blue), n + 1 (sky blue), n + 2 (gray), n + 3 (pink), n + 4 (yellow), n + 5 (wine red), and n + 6 (purple). Extensive contacts are formed between subunits n (blue) and n + 3 (pink), providing layer-to-layer stability. The extent of these contacts is partially determined by the rotation angle between subunits (subunits per turn), which defines the potential overlap region between layers. Staples that extend from n + 4 back to n (CS20 and P pili) are marked with black arrows.

- (B) Contacts to subunit n are shown as spheres, with colors corresponding with the subunit number from (A).
- (C) Contacts to subunit n are shown with subunits rotated 90° about the horizontal axis.
- (D) Contact regions are shown in yellow, with loops that extend from the central β-strands back to subunit n 2 marked by magenta arrows. Scale bars in (A) and (B-D) (shown in [D]) are 10 Å. CFA/I, CS17, CS20, P pili, type 1 PDB: 8EHR, 8EHS, 8EHT, 5FLU, and 6Y7S, respectively. See also Video S1.

During our helical processing workflow, we searched for the optimal helical parameters for each filament. Based on these calculations, CFA/I has a helical rise of 8.51 Å and a twist of 113.4°, which is very similar to the rise of 8.43 Å and twist of 113.2° calculated for CS17. Not surprisingly, because of CS20's differences in subunit size and subunit-to-subunit interactions, it also has changes to its helical parameters, with an increase of 8.95 Å and a twist of 111.8°. Overall, our cryo-EM structures indicate that, although CS20 colonizes the gut, as do CFA/I and CS17, it retains structural properties that make it unique for this niche.

By determining the structures of the ETEC adhesion pili CFA/I, CS17, and CS20, we reveal that, despite operating on bacteria in the same environment, filaments can possess distinct structural features. To further explore how adhesion pili can adapt their structures, we expanded our comparisons to include two adhesion pili that have been previously solved by cryo-EM, P pili (PDB: 5FLU) and type 1 pili (PDB 6Y7S), which are found on UPEC bacteria that colonize the urinary tract. Although they share a common architecture, each filament contains unique molecular contacts. For all five pili, a subunit's interaction with

its layer-to-layer neighbor (n to n + 3) stabilizes the helical filament. P pili have the smallest rotation angle per subunit; therefore, the third subunit does not come in full contact with the layer above (Figure 2 and Video S1). CS20, with the largest rise per subunit, has long loops that form contacts between layers, but lacks the extensive close contacts to n + 3 observed in type 1 pili. In all five pili except P pili, a loop region extends up and back from subunit n + 2 to contact subunit n (Figure 2D). This loop is composed of residues 69-77, 70-76, 89-94, or 90-94, for CFA/I, CS17, CS20, or type 1 pili, respectively.

Toward our goal of determining the relationship between the molecular contacts described above and the biophysical properties that allow adhesion pili to function in their environmental niches, we measured their unwinding forces using optical tweezers force spectroscopy studies.

Filament unwinding by force spectroscopy

Optical tweezers force measurements applies tensile force to a pilus, allowing us to assess if filaments exhibit superelastic behavior, that is, if the filament can be extended via phase

Structure Article



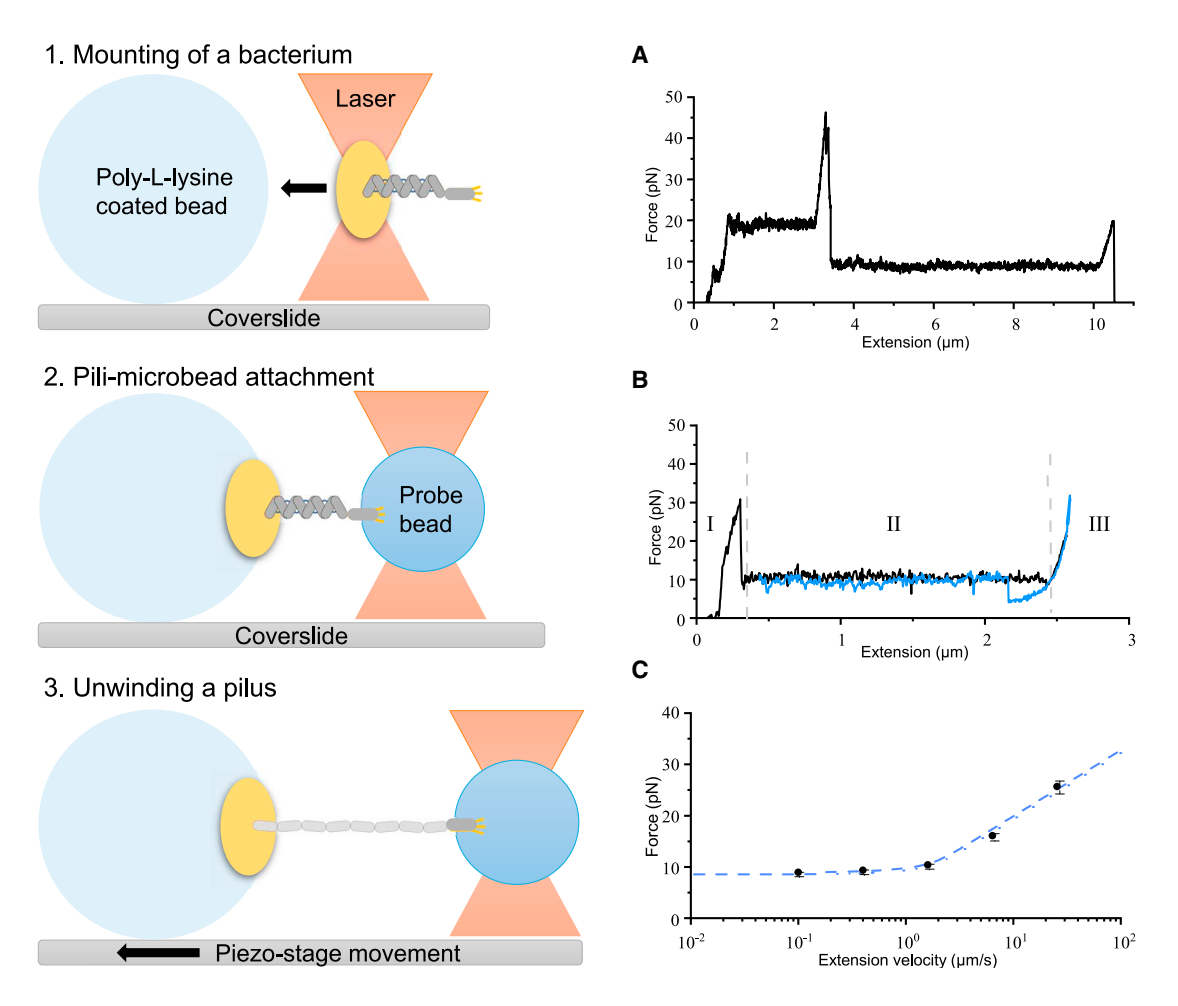


Figure 3. Force measurements of CS17 pili

(A) (Left) The procedure of an optical tweezers force measurement. Mounting and measuring procedures. (1) First, we mount a bacterium to a 10-µm poly-L-lysine coated bead that is immobilized on the coverslide. The coated bead serves as a mount for a bacterium. A bacterium is thereafter trapped in the optical tweezers and attached to the coated bead. (2) Second, a 2-µm probe bead is trapped and the trap stiffness is calibrated using the power spectrum method.²⁵ After calibration, the probe bead is brought close (~1-2 µm) to the mounted bacterium using a piezo-stage. When a pilus attaches, the motion of the probe bead changes from the equilibrium position, which is seen in the live camera image and the real-time force response. (3) Finally, with a pilus attached, we move the piezo-stage at 0.1 µm/s while keeping the trap stationary. This applies tensile force to a pilus as the bacterium and probe bead are separated. A force response of pili is shown in (A). First, two pili are bound, so the force is double. After one pilus detached (~3.5 μm, the unwinding force, and filament extension, are for one pilus

(B) Pilus unwinding has three distinct regions, as described in the text. Pilus rewinding (blue curve) begins with a dip in force, until a layer-to-layer interaction allows a constant-force rewinding.

(C) DFS data fitted with the sticky-chain model.

transitions and relaxed back to its original shape without structural damage. In addition, we use these measurements to quantify biophysical features such as the unwinding force. These data are currently available for CFA/I, CS20, P pili, and type 1 pili²²⁻²⁴ (see Table S4). An illustration of how to measure the unwinding force of a pilus with optical tweezers is shown in the left panel of Figure 3 and typical force-extension responses of CS17 pili are shown in Figures 3A and 3B. Since a bacterium expresses a multitude of pili of different lengths, occasionally two or more pili can attach to the probe bead, so that several pili are being extended initially. Since the force response of two or more pili are a multiple of one, we easily observed when the response came from one pilus. Figure 3A shows the force response with two pili attached, and then one detaches (at 2.7 μm), leaving a single attached CS17 pilus. In Figure 3B, we show the response of a single pilus, where the unwinding and rewinding phases are represented by the black and blue curves, respectively. To ensure that the force responses were not measured in a dynamic regime, we performed experiments at steady state (equilibrium conditions),26 as demonstrated by the overlapping of the unwinding and rewinding curves in Figure 3B.

Based on the literature regarding other helix-like adhesion pili^{27,28} and previously characterized ETEC pili,^{22,23} we observed that CS17 pili also showed a three-region force-extension/ contraction response. Thus, our force data confirm the structural analysis that CS17 pili exhibit a helix-like structure that is superelastic and can thereby rewind when tensile stress is removed. The force-response can be explained by tensile stress that first



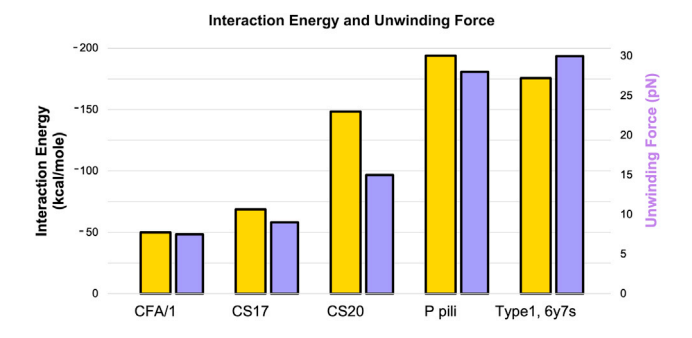


Figure 4. The force of pilus unwinding correlates with interaction en-

The force required to unwind a pilus (purple) increases as the interaction energy between layers (n to n + 3 and n + 4) increases (gold). The interaction energy associated with the staple accounts for the majority of the interaction energy for CS20 (-103 kcal/mol), with a smaller contribution by the staple for P pili (-42 kcal/mol).

elongates the pilus by increasing the force linearly (region I). Sequential unwinding of the structure (between the dashed lines) then gives rise to a constant force plateau (region II) in which the average is the unwinding force. The overshooting force ramp from 10 to 30 pN during an extension of approximately 0.3 µm is not a part of the plateau and will not affect the unwinding force measurement, since only data between the dashed vertical lines represents the true unwinding force. After analyzing the force response of individual CS17 pili (n = 40) we measured an average unwinding force of 9 ± 1 pN (mean \pm standard deviation).

Once a pilus is unwound, it is possible to further stretch the structure, which is indicated by the second region of linearly increasing force (region III). The force response of CS17 further indicates its helix-like structure, as supported by the discrepancy seen between the extension and contraction curves at approximately 2.25 µm in Figure 3B; a dip in the force response during contraction (pilus rewinding) indicates that major subunits are stacked in a helical structure that must be re-initiated for continued rewinding.²⁹

Biophysical characterization of CS17 pili

To investigate the dynamic behavior of CS17 pili as well as identify their biophysical parameters, we performed dynamic force spectroscopy (DFS) measurements. In a DFS measurement, a pilus is extended with increasing velocity in cycles and the average unwinding force of region II is recorded. This forces subunit-subunit interactions to break under non-equilibrium conditions.²⁶ Figure 3C shows the mean unwinding forces vs the unwinding velocity for CS17 pili (n = 13). As seen, the pilus responses at low extension velocities (< ~1.5 μm/s) remained constant, with the unwinding force essentially identical to that measured for the steady-state force. For higher velocities (> 1.5 µm/s) the unwinding force increased logarithmically with increasing velocities. Both the steady-state force response and the dynamic force response of a helix-like pilus can be well modeled by the sticky-chain model.²⁴ The sticky-chain model is an analytical model that describes the structural response of helix-like polymers under tensile force, in which force-assisted subunit-to-subunit bond breaking follows Bell's law. 30

A transition point that separates the steady-state and dynamic region is denoted as the pilus corner velocity (L^{*}) . The corner velocity is defined as the maximum extension velocity of a pilus before any increase in velocity leads to an increased unwinding force. For velocities less than the corner velocity, pili unwound independent of extension speed, whereas for velocities above the corner velocity $(L > L^*)$, the unwinding force increased logarithmically with increasing velocity.31 The logarithmic increase in force vs extension velocity relationship, can further be used to assess the bond length (Δx_{AT}), which is the distance from the energy minimum to the transition barrier maximum of the layer-to-layer bond. See Methods for a description.

Thus, to quantify the corner velocity, $\dot{\mathcal{L}}^*$, and the bond length, Δx_{AT} , we plotted the mean unwinding force vs the unwinding velocity (Figure 3C) and fitted the sticky-chain model. The black dots (bars represent one standard deviation) in Figure 3C show the mean unwinding forces at different velocities, whereas the blue dashed line indicates a fit to the full set of rate equations at T set to 298 K. The best fit of the model to the experimental data yielded the corresponding model parameters: $L^{*} = 1220 \pm 140$ nm/s and $\Delta x_{AT} = 0.74 \pm 0.08$ nm. To further relate how these biophysical properties, in particular the unwinding force of the different pili types, correlate with the unique molecular contacts that stabilize the quaternary structure, we next calculated intra-filament interaction energies for all pili.

Interaction energies correlate with pili unwinding force

Calculations of interaction energies between pilin subunits allow us to estimate the strength of interactions within filaments. The NAMD energy plugin in VMD³² calculates both van der Waals interactions and electrostatic interactions. While we are not calculating binding free energy, our values do reflect the strength of the interaction between pilin subunits. In particular, we are interested in the strength of dissociation during unwinding. During this process subunits are initially associated, and the interactions then dissociate under force (subunits unpeel from the filament). As seen in Figures 4 and S3 and Table S4. There are strong layer-to-layer interactions between subunits n and n + 3, with favorable energies of interaction, -43, -62, -46, -105, and -165 kcal/mol for CFA/I, CS17, CS20, P pili, and type 1, respectively. The most favorable layer-to-layer interaction energy, in type 1 pili, may result from the combination of a smaller rise and a larger rotation per subunit; we note that openings from the outside milieux to the internal central cavity that are present in all five pili are minimized in type 1 pili, because of its more compact filament structure (33 and PDB: 6Y7S). The N-terminal extension of the n+4 subunit that sits in the groove of subunit n + 3 contributes -7, -7, and -10 kcal/mol, for CFA/I, CS17, and type 1 pili, respectively, and is a dominant contributor to the energy of interaction for CS20 and P pili, but for distinct reasons. CS20 has no contribution from the n + 4 residues that fill the n + 3 groove, and a large contribution (-103 kcal/mol) from the staple that extends beyond the groove up to subunit n. Conversely, P pili have similar contributions from its groove residues (-47 kcal/mol) and its staple (-42 kcal/mol). The correlation between interaction energy and unwinding force is statistically verified by a linear fit to a scatterplot of the maximum values of interaction energies and unwinding force, which gives a Pearson correlation coefficient of 0.93 (Figure S3). We note that removal of the staple interactions decreased the interaction energies of CS20 and P pili (Table S4), emphasizing

Article



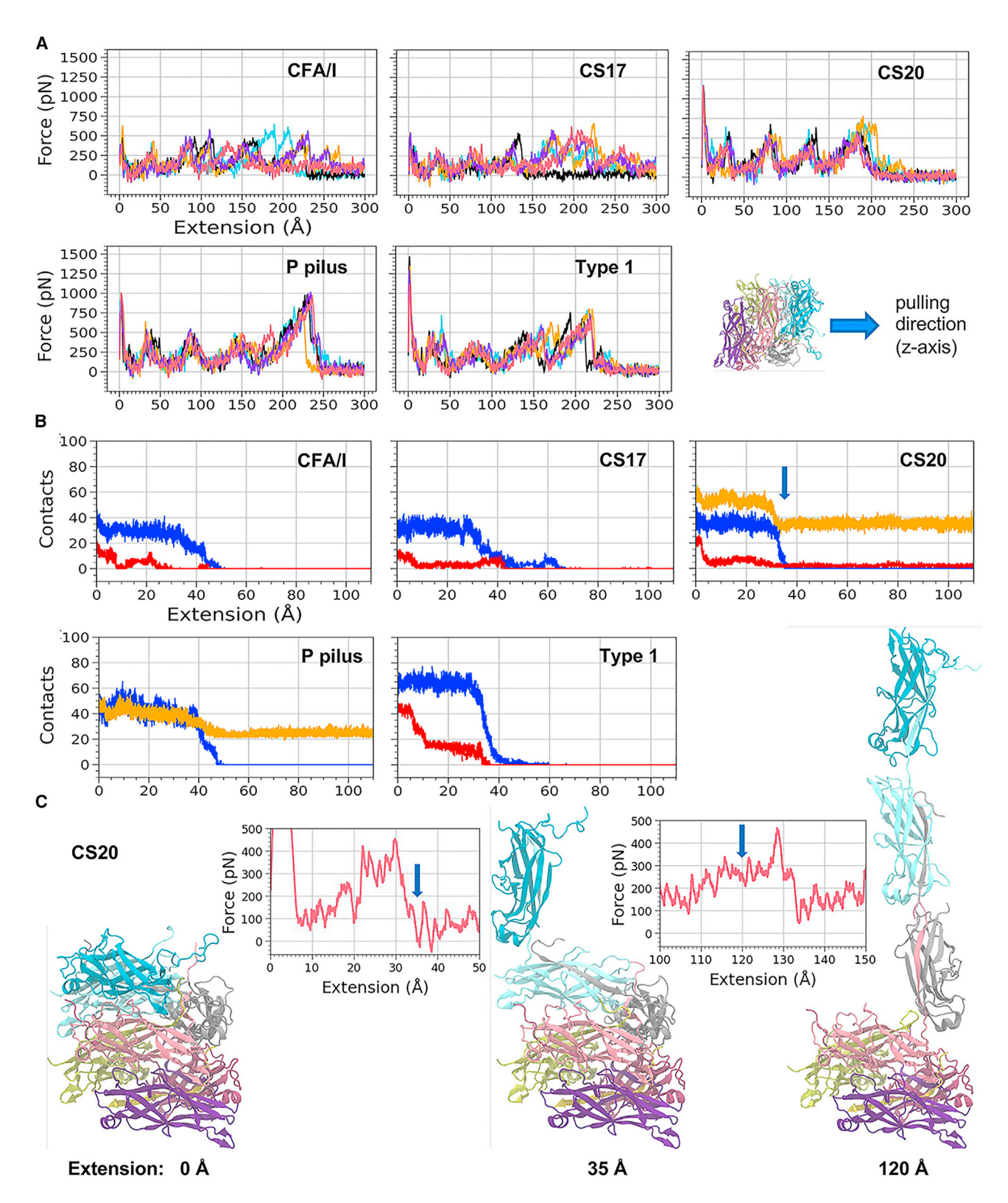


Figure 5. sMD simulations describe molecular events of pilus unwinding

(A) Force vs extension curves are shown for each of the five systems discussed, CFA/I, CS17, CS20, P pili, and type 1. The colors represent the multiple trials of each system (five trials; pink = trial 1). Force data are a 1-ns running average. Also, an image of the 7mer indicating the pulling direction is shown.

(B) Contacts are shown between structural components of pilin subunits are shown for each of the five systems: layer-to-layer interactions between subunits 2 and 5 (blue curves; subunit 1 is the tip subunit), contacts between the loop region of subunit 4 and all other subunits (red curves), and contacts between the staple





the importance of the staple interactions for P pilus and CS20 stability.

The interaction energy between subunits is not the only parameter that will influence the force needed to unwind pili. Additional entropic factors, such as the solvation energy, also influence the unwinding force. To measure an estimate of the entropic contribution to pilus unwinding, we calculated the buried surface area of the interacting pilus subunits using COCOMAPS³⁴ (see Table S4), as done previously for P pili⁸ and type 1 pili. 33 Subsequently, we tested our values for correlation to unwinding forces and other pilin properties. Our findings indicate that, as expected, the total buried surface areas of subunit n to n + 3 and n + 4 correspond with some degree with the size of the individual subunits. Here, CFA/I and CS17 have smaller buried surface area and molecular weights (1189, 1251 Å² and 15.0, 15.3 kDa, respectively), while those of CS20, P pili, and type 1 are larger (1737, 1635, 1625 Å² and 17.5, 16.6, and 15.8 kDa, respectively). These values support a trend where pili with larger subunits and thus larger buried surface require a greater force to unwind. Next, to gain an atomic understanding of filament unwinding and the subsequent breakage of the inter-subunit molecular contacts described in our interaction energy calculations, we performed sMD simulations.

Filament unwinding by sMD simulations

To examine filament unwinding under force, sMD was performed for each of the five pilus systems, CFA/I, CS17, CS20, P pilus, and type 1. The resulting force vs extension profiles are shown in (Figure 5A) (P pilus simulations shown here were previously reported in⁹). The sMD simulations can be broadly classified into two main categories by the observed force vs extension profile patterns: (1) profiles with an initial sharp peak representing the tip subunit unwinding from the helical filament, followed by three peaks corresponding with the breakage of sequential layer-to-layer interactions, followed by a final peak indicating a subunit being removed from the filament due to filament breakage, and (2) profiles with resolvable peaks during initial filament extension but that become more variable at higher values of the filament extension. CS20, P pilus, and type 1 comprise the first category, while the second category consists of CFA/I and CS17. CS20, P pili, and type 1 all contain a disulfide bond as part of the pilin structure, while CFA/I and CS17 both lack this bond. We see that the overall level of force required to extend CFA/I and CS17 filaments in the sMD simulations is lower than the level of force required for the other three systems, which is consistent with the observations in Table S4 and Figure 3 that the force of unwinding is smaller for CFA/I and CS17 compared with the other three systems. This is similarly seen by integrating the force-extension curves to obtain the nonequilibrium work shown in Figure S5. While the force in sMD cannot be directly compared with optical tweezers force

measurements since the pulling velocities (loading rates) in sMD are significantly higher (nonequilibrium conditions), the nonequilibrium conditions of sMD do not hinder our ability to obtain valuable insights into the dynamic structural changes for the five studied pilus types that occur during sMD force experiments.

Further, we measured contacts between various regions of the simulated systems. Specifically, we monitored layer-to-layer contacts, staple contacts, and the loop/subunit contacts. Since we simulated 7mer filaments, we calculated contacts for the layer-to-layer interaction between subunits 2 and 5 (numbering with subunit 1 as the filament tip subunit). For staple interactions we monitored the staple of subunit 6 in P and CS20 pili, and for the loop/subunit interactions we monitored the loop region in subunit 4 of CFA/I, CS17, CS20, and type 1 pili. Overall we observed that layer-to-layer contacts, staple contacts, and loop/subunit contacts decrease roughly simultaneously. In Figure 5 and in Figure S4, we saw the greatest variation of contact breakages across simulation trials for CFA/I and CS17. This variability during unwinding is consistent with the large variation in force vs extension patterns observed by sMD. Data are shown to 100 Å filament extension; in some trials, CFA/I initial layerto-layer contacts were not fully disrupted until that distance. The type 1 pilus has the greatest number of layer-to-layer contacts, and the number decreases sharply to zero as the layer unwinds (Figure 5B, blue curves). For the P pilus and CS20 pilus with the staple present, we note that the staple contacts are not expected to drop to zero because subunit 6 is restrained in the simulation. Therefore, even after the nearby layer-to-layer interactions between subunit 5 and subunit 2 were broken, the staple from subunit 6 remained in its original orientation. However, we clearly observed that the total number of staple contacts to all subunits decreased as the layer-to-layer interactions (subunit 2 to subunit 5) were broken (Figure 5B and S4, orange curves). For CFA/I, CS17, CS20, and type 1, we observed that the contacts made by the loop of subunit 4 with all other subunits were broken by the time that the subunit 2 to subunit 5 laverto-layer interactions released (Figures 5B and S4, red curves). Several representative snapshots from the first trial of the CS20 sMD simulation are shown in Figure 5C. Additionally, Figure 5C shows inset snapshots of the force vs extension curves of a CS20 sMD simulation, demonstrating drops in the force as layers are unwound. The left inset image also shows that the position where the force drops at around 35 Å corresponds with the contact loss for CS20 observed in Figure 5B. Videos of all sMD trials are included in the Supplemental Information to depict the trajectories for each simulation (Videos S2, S3, S4, S5, and S6).

In summary, the sMD simulation results demonstrate at the molecular scale that all three modes of subunit-subunit contacts (layer to layer, staple, and loop) contribute to the unwinding mechanism, and our simulations underscore the importance of

region of subunit 6 and all other subunits (orange curves). The loop and staple regions for each system are defined as in the text. Data are plotted to 100 Å of filament extension. Contact data are shown for trial 1 of each simulation in this figure, and the contact data for the additional trials are included in the supplemental information. Contact data are a 5-ns running average.

⁽C) Three representative snapshots from the CS20 sMDs simulation (trial 1), depicting how a typical unwinding trajectory occurs. Shown are the initial CS20 structure (left), the structure once the first subunit has been unwound from the filament (middle), and the structure once three subunits have been unwound from the filament (right). Inset images show the force vs extension data for trial 1 of the CS20 filament in the vicinity of 35 Å and 120 Å. Vertical arrows indicate these contacts (B) and force (C) for CS20 trial 1.

Article



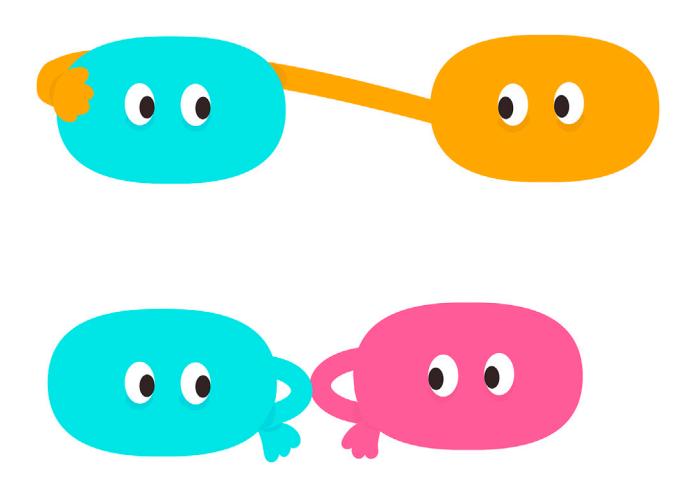


Figure 6. Interactions can be from near or far subunits

Subunit-subunit interactions that must be broken for filament unwinding can be from a staple far away (top panel, textitn to n + 4 and n + 5) or from extended loops on closer subunits (bottom panel, n to n + 2). Illustration by Siriratt Thairatana.

the disulfide bond for the stability of pilin subunits unwinding under high loading rates.

DISCUSSION

Bacteria known to cause urinary tract or gastrointestinal tract diseases express adhesion pili that must mediate adhesion in significantly different environments. The extent to which the environment or genetics dictate the properties of these pili is not known. To address this question, we used a multimodal approach to investigate the interplay between class 1 and class 5 pili genetic, structural, and biophysical properties, as well as mechanistic details of unwinding.

Interestingly, we found that the genetic similarities are much weaker than expected, especially within classes. These findings are supported by data shown in Table 1 and Figure S1, with genetic similarities ranging from 30% to 69%. To examine the structural differences between the pili we performed cryo-EM on CFA/I, CS17, and CS20 pili, all from ETEC. As seen in Table S2, the alpha carbon backbones of these pilin subunits, along with those of P pili and type 1 from UPEC, vary by 1.3-19.1 Å. While the subunit RMSD of CFA/I to CS17 pili is 1.3 Å and that of CFA/I to CS20 is 17.3, Å, CS17 to CS20 is only 6.6 Å. This disparity of RMSD values is surprising; the packing of subunits into a helical filament is reasonably similar for all three pili, with their rise per subunit ranging from 8.5 Å to 9.0 Å and their helical twist ranging from 112° to 114° per subunit. More significant differences are observed when these pili are compared with UPEC P pili and type 1 pili (see Table S2). Structural differences include the presence (CS20, Ppili) or absence (CFA/I, CS17, type 1) of a staple region that connects distant subunits and the presence (CS20, P pili, type 1) or absence (CFA/I, CS17) of an internal disulfide bond, as seen in Figure 2C and Video S1. The internal disulfide bond has been determined via sMD simulations to be a critical component for subunit structural integrity under high tensile force. Thus, filaments possess differing structural features, irrespective of the bacterial environment.

We next investigated correlations between the structures and biophysical properties of adhesion pili. As seen in Figure 4, Table S4, and Figure S3, our results show a significant correlation between layer-to-layer interaction energies and the force required to unwind pili from their helical to fibrillar architecture. In addition, we see a strong correlation between the force required to unwind pili and the biophysical parameter, corner velocity (Table S4). The corner velocity provides information of a pilus structure response to extension velocity, in which the force response is velocity-independent below the corner velocity. Using P as the reference (400 nm/s), ETEC related pili show 2-3 times higher values, whereas type 1 is exceptionally low (6 nm/s). It was further found that the N-terminal staple regions of CS20 and P pili contribute to their interaction energies and thus to filament stability, with the CS20 staple contributing twothirds of the interaction energy while in P pili the staple contribution is only one-quarter of the total energy. We expect this is due to the staple region of CS20 providing layer-to-layer interactions that are lacking between subunits n and n + 3. P pili do have more of these interactions, and therefore the staple region need not be as dominant. Interaction energies and unwinding forces are smaller for CFA/I and CS17, which we expect to be due, in part, to lack of a staple. Even without a staple, energies are larger in type 1 pili, likely in part because of the very strong n to n + 3 interactions. As diagrammed in Figure 6, we conclude that interactions of the staple region to subunits that are more than one helical turn away (n to n + 4 and n + 5) can be partially compensated for by loop/subunit interactions from a closer neighbor.

In addition to the interaction energies, we also calculated the buried surface area between interacting subunits to gain insight into the entropic contributions of filament unwinding. We find that the pili with smaller subunits, CFA/I and CS17, have a smaller buried surface area, while the pili with larger subunits display larger buried surface areas. Even though these values do not have as strong of a correlation with the unwinding force compared with the calculated interaction energies (see Figure S3), they point to a trend where filaments with larger subunits unwind at greater forces. This is most likely due to the fact that breaking the subunit-subunit interactions between the larger subunits during unwinding would impose a larger entropic solvation penalty compared with the smaller subunits. Despite CS20 having the largest buried surface area and mass of the five pili considered here, its unwinding force is only approximately one-half of the measured force for P pili and type 1 pili. This is most likely due to its smaller interaction energy, especially once the staple contacts are broken. This suggests that the relative contributions of protein-protein interaction energy and solvation effects are tuned for specific bacterial environments, thereby optimizing the molecular mechanisms that govern the filament unwinding force. Thus, molecular parameters such as subunit size and the make-up of subunit-subunit interactions establish the precise mechanisms that modulate unwinding force for pili to operate in their respective environment.

How does filament unwinding under tensile force then proceed? Structural data suggest that interacting loops extending from the central β-strands of the pilins provide loop-subunit interactions that must be broken during pilus unwinding and restored during rewinding (Figure 2D). To elucidate mechanistic details of unwinding we used sMD simulations, which show that





there is an unpeeling of subunits from a filament when tensile stress is applied. The tongue-in-groove n to n+1 attachment is maintained, while bonds to n+2 and n+4 are broken and the interaction between the n and n+3 subunits unpeels.

What dictates the intermediate unwinding force of CS20 pili as compared with other ETEC and UPEC pili? The genetic sequence of ETEC-expressed CS20 pili defines them as class 1 pili, yet they have an unwinding force half that of the other (UPEC) class 1 pili that have been studied, and twice that of ETEC class 5 pili. These intermediate properties of CS20 pili provide clues to the tuning of pilus structures to maximize sustained bacterial adhesion. While both the interactions energies and unwinding forces are increased in CS20 pili relative to the other ETEC pili reported here, there is a significant decrease in the layer-to-layer interactions between CS20 pilin subunits n and n + 3, as compared with P pili. These decreases seem to be due to the larger rise per subunit of CS20 and the overtwisting of the assembled filament, due to a larger rotation angle per subunit. Type 1 pili, found in both UPEC and ETEC, have no staple region. Their biophysical properties seem to arise from a more compact filament structure and the greatest number of layer-to-layer contacts between pilins n and n + 3, resulting in the highest interaction energy and the highest unwinding force of the pili investigated.

Thus, our cryo-EM data, in combination with genetic data, optical tweezers force results, and sMDs simulations, show that pilin subunit structures are tuned to provide mechanical solutions for pilus stability that suit their preferred microenvironment. Pili have three structural solutions for stabilizing the filaments: the n to n+3 layer-to-layer interactions, the staple region interactions, and extended loops from close neighbors. Improved understanding of the tuning of structural and biophysical properties of pili can aid in current and future development of ETEC pili as vaccine target antigens. 35,36

STAR*METHODS

Detailed methods are provided in the online version of this paper and include the following:

- KEY RESOURCES TABLE
- RESOURCE AVAILABILITY
 - Lead contact
 - Materials availablity
 - O Data and code availability
- EXPERIMENTAL MODEL AND SUBJECT DETAILS
- METHOD DETAILS
 - O Sample preparation for cryo-EM
 - Cryo-EM data collection and processing
 - Model building for the filaments
 - O Interaction energy and buried surface area calculations
 - Filament unwinding using optical tweezers
 - Description of the sticky-chain model
 - Molecular dynamics simulations
- QUANTIFICATION AND STATISTICAL ANALYSIS

SUPPLEMENTAL INFORMATION

Supplemental information can be found online at https://doi.org/10.1016/j.str. 2023.03.005.

ACKNOWLEDGMENTS

Supported by NIH/NIAID grant R21 Al156236 (E.B.); NIH/NIGMS grant U24 GM116789 (multi-Pl, including E.B. and Dr. Wen Jiang); the Swedish Research Council (2019-04016) to M.A.; NSF Grant MCB-1817670 (J.L.B.); use of the Electronic Laboratory for Science and Analysis (ELSA) high-performance computing cluster at The College of New Jersey for conducting the molecular dynamics simulations, funded, in part, by NSF Grants OAC-1826915 and OAC-1828163; J.L.B. is also a member of the MERCURY Consortium, NSF grant CHE-2018472. Thanks to Siriratt Thairatana for her illustrations.

AUTHOR CONTRIBUTIONS

E.B., M.A., and J.L.B. conceived the study and designed the experiments. All authors conducted experiments, analyzed data, and contributed to all drafts of the manuscript.

DECLARATION OF INTERESTS

The authors declare that they have no known competing financial interests or personal relationships that could have appeared to influence the work reported in this paper.

INCLUSION AND DIVERSITY

We support inclusive, diverse, and equitable conduct of research.

Received: November 14, 2022 Revised: January 18, 2023 Accepted: March 6, 2023 Published: March 30, 2023

REFERENCES

- Bekeredjian-Ding, I. (2020). WHO Product Development for Vaccines Advisory Committee (PDVAC) Virtual Consultation 4: Update on Development of Enterotoxigenic E.Coli (ETEC) Vaccines 18 June 2020.

 Tech. Rep.. https://cdn.who.int/media/docs/default-source/immunization/pdvac/2020/pdvac_etec_18-june_executive-summary.pdf?sfvrsn=be14cf12_
- Colombara, D.V., Khalil, I.A.M., Rao, P.C., Troeger, C., Forouzanfar, M.H., Riddle, M.S., and Mokdad, A.H. (2016). Chronic health consequences of acute enteric infections in the developing World. Am. J. Gastroenterol. Suppl. 3, 4–11. https://doi.org/10.1038/ajgsup.2016.9.
- Troeger, C., Colombara, D.V., Rao, P.C., Khalil, I.A., Brown, A., Brewer, T.G., Guerrant, R.L., Houpt, E.R., Kotloff, K.L., et al. (2018). Global disability-adjusted life-year estimates of long-term health burden and undernutrition attributable to diarrhoeal diseases in children younger than 5 years. Lancet. Glob. Health 6, e255–e269. https://doi.org/10.1016/S2214-109X(18)30045-7.
- Guerrant, R.L., DeBoer, M.D., Moore, S.R., Scharf, R.J., and Lima, A.A.M. (2013). The impoverished gut—a triple burden of diarrhoea, stunting and chronic disease. Nat. Rev. Gastroenterol. Hepatol. 10, 220–229. https:// doi.org/10.1038/nrgastro.2012.239.
- Lee, G., Paredes Olortegui, M., Peñataro Yori, P., Black, R.E., Caulfield, L., Banda Chavez, C., Hall, E., Pan, W.K., Meza, R., and Kosek, M. (2014). Effects of Shigella-campylobacter- and ETEC-associated diarrhea on childhood growth. Pediatr. Infect. Dis. J. 33, 1004–1009. https://doi.org/ 10.1097/INF.00000000000000351.
- Choudhury, D., Thompson, A., Stojanoff, V., Langermann, S., Pinkner, J., Hultgren, S.J., and Knight, S.D. (1999). Structure of the FimC-FimH chaperone-adhesin complex from uropathogenic Escherichia coli. Science 285, 1061–1066. https://doi.org/10.1126/science.285.5430.1061.
- Bullitt, E., and Makowski, L. (1995). Structural polymorphism of bacterial adhesion pili. Nature 373, 164–167. https://doi.org/10.1038/373164a0.
- 8. Hospenthal, M.K., Redzej, A., Dodson, K., Ukleja, M., Frenz, B., Rodrigues, C., Hultgren, S.J., DiMaio, F., Egelman, E.H., and Waksman,

Article



- G. (2016). Structure of a chaperone-usher pilus reveals the molecular basis of rod uncoiling. Cell 164, 269-278. https://doi.org/10.1016/j.cell.2015.
- 9. Dahlberg, T., Baker, J.L., Bullitt, E., and Andersson, M. (2022). Unveiling molecular interactions that stabilize bacterial adhesion pili. Biophys. J. 121, 2096-2106. https://doi.org/10.1016/j.bpj.2022.04.036.
- 10. Smith, E.M., Grassel, C.L., Papadimas, A., Foulke-Abel, J., and Barry, E.M. (2022). The role of CFA/I in adherence and toxin delivery by ETEC expressing multiple colonization factors in the human enteroid model. PLoS Negl. Trop. Dis. 16, e0010638. https://doi.org/10.1371/journal.pntd.
- 11. Sheikh, A., Rashu, R., Begum, Y.A., Kuhlman, F.M., Ciorba, M.A., Hultgren, S.J., Qadri, F., and Fleckenstein, J.M. (2017). Highly conserved type 1 pili promote enterotoxigenic E. coli pathogen-host interactions. PLoS Negl. Trop. Dis. 11, e0005586.
- 12. Spaulding, C.N., Schreiber, H.L., 4th, Zheng, W., Dodson, K.W., Hazen, J.E., Conover, M.S., Wang, F., Svenmarker, P., Luna-Rico, A., et al. (2018). Functional role of the type 1 pilus rod structure in mediating host-pathogen interactions. Elife 7, e31662. https://doi.org/10.7554/
- 13. Miller, E., Garcia, T., Hultgren, S., and Oberhauser, A.F. (2006). The mechanical properties of E. coli type 1 pili measured by atomic force microscopy techniques. Biophys. J. 91, 3848-3856. https://doi.org/10.1529/ biophysj.106.088989.
- 14. Zakrisson, J., Wiklund, K., Axner, O., and Andersson, M. (2013). The Shaft of the type 1 fimbriae regulates an external force to match the FimH catch bond. Biophys. J. 104, 2137-2148. https://doi.org/10.1016/j.bpj.2013. 03.059.
- 15. Thomas, W.E., Vogel, V., and Sokurenko, E. (2008). Biophysics of catch bonds. Annu. Rev. Biophys. 37, 399-416. https://doi.org/10.1146/annurev.biophys.37.032807.125804.
- 16. Nuccio, S.-P., and Bäumler, A.J. (2007). Evolution of the chaperone/usher assembly pathway: fimbrial classification goes Greek. Microbiol. Mol. Biol. Rev. 71, 551-575. https://doi.org/10.1128/MMBR.00014-07.
- 17. D. Low, B. Braaten, Van Der Woude., M.W. Fimbriae, F.C. Neidhardt, R. Curtiss, III, J.L. Ingraham, E.C.C. Lin, K.B. Low, and B. Magasanik, et al., eds. (1996). Escherichia coli and Salmonella: cellular and molecular biology, 2nd ed., AS 146-157.
- 18. Anantha, R.P., McVeigh, A.L., Lee, L.H., Agnew, M.K., Cassels, F.J., Scott, D.A., Whittam, T.S., and Savarino, S.J. (2004). Evolutionary and functional relationships of colonization factor antigen I and other class 5 adhesive fimbriae of enterotoxigenic Escherichia coli. Infect. Immun. 72, 7190-7201. https://doi.org/10.1128/IAI.72.12.7190-7201.2004.
- 19. Girardeau, J.P., Bertin, Y., and Callebaut, I. (2000). Conserved structural features in class I major fimbrial subunits (pilin) in Gram-negative bacteria. Molecular basis of classification in seven subfamilies and identification of intrasubfamily sequence signature motifs which might be implicated in quaterna. J. Mol. Evol. 50, 424-442.
- 20. Zivanov, J., Nakane, T., Forsberg, B.O., Kimanius, D., Hagen, W.J., Lindahl, E., and Scheres, S.H. (2018). New tools for automated high-resolution cryo-EM structure determination in RELION-3. Elife 7, 421666e42222. https://doi.org/10.7554/eLife.42166.
- 21. Barnhart, M.M., Sauer, F.G., Pinkner, J.S., and Hultgren, S.J. (2003). Chaperone-subunit-usher interactions required for donor strand exchange during bacterial pilus assembly. J. Bacteriol. 185, 2723-2730. https://doi.org/10.1128/JB.185.9.2723-2730.2003.
- 22. Andersson, M., Björnham, O., Svantesson, M., Badahdah, A., Uhlin, B.E., and Bullitt, E. (2012). A structural basis for sustained bacterial adhesion: biomechanical properties of CFA/I pili. J. Mol. Biol. 415, 918-928. https://doi.org/10.1016/j.jmb.2011.12.006.
- 23. Mortezaei, N., Epler, C.R., Shao, P.P., Shirdel, M., Singh, B., McVeigh, A., Uhlin, B.E., Savarino, S.J., Andersson, M., and Bullitt, E. (2015). Structure and function of enterotoxigenic E scherichia coli fimbriae from differing assembly pathways. Mol. Microbiol. 95, 116-126. https://doi.org/10.1111/ mmi.12847.

- 24. Andersson, M., Fällman, E., Uhlin, B.E., and Axner, O. (2006). A sticky chain model of the elongation and unfolding of Escherichia coli P pili under stress. Biophys. J. 90, 1521-1534. https://doi.org/10.1529/biophysj.105. 074674.
- 25. Tolić-Nørrelykke, S.F., Schäffer, E., Howard, J., Pavone, F.S., Jülicher, F., and Flyvbjerg, H. (2006). Calibration of optical tweezers with positional detection in the back focal plane. Rev. Sci. Instrum. 77, 103101. https:// doi.org/10.1063/1.2356852.
- 26. Andersson, M., Fällman, E., Uhlin, B.E., and Axner, O. (2006). Dynamic force spectroscopy of E. coli P pili. Biophys. J. 91, 2717-2725. https:// doi.org/10.1529/biophysj.106.087429.
- 27. Axner, O. (2010). Single molecule spectroscopy in Chemistry, physics and biology. In Springer Series in Chemical Physics, 96 (Springer Berlin Heidelberg). http://link.springer.com/10.1007/978-3-642-02597-6.
- 28. Axner, O. (2011). In Assessing Bacterial Adhesion on an Individual Adhesin and Single Pili Level Using Optical Tweezers, 1st edn, D. Linke and A. Goldman, eds. (Springer) http://link.springer.com/10.1007/978-94-007-0940-9 19.
- 29. Lugmaier, R.A., Schedin, S., Kühner, F., and Benoit, M. (2008). Dynamic restacking of Escherichia coli P-pili. Eur. Biophys. J. 37, 111-120. https://doi.org/10.1007/s00249-007-0183-x.
- 30. Bell, G.I. (1978). Models for the specific adhesion of cells to cells: a theoretical framework for adhesion mediated by reversible bonds between cell surface molecules. Science 200, 618-627.
- 31. Castelain, M., Ehlers, S., Klinth, J., Lindberg, S., Andersson, M., Uhlin, B.E., and Axner, O. (2011). Fast uncoiling kinetics of F1C pili expressed by uropathogenic Escherichia coli are revealed on a single pilus level using force-measuring optical tweezers. Eur. Biophys. J. 40, 305-316. https:// doi.org/10.1007/s00249-010-0648-1.
- 32. Humphrey, W., Dalke, A., and Schulten, K. (1996). VMD: visual molecular dynamics. J. Mol. Graph. 14, 33-38,27-28. https://doi.org/10.1016/0263-7855(96)00018-5.
- 33. Hospenthal, M.K., Zyla, D., Costa, T.R.D., Redzej, A., Giese, C., Lillington, J., Glockshuber, R., and Waksman, G. (2017). The cryoelectron microscopy structure of the type 1 chaperone-usher pilus rod. Structure 25, 1829-1838.e4. https://doi.org/10.1016/j.str.2017.10.004.
- 34. Vangone, A., Spinelli, R., Scarano, V., Cavallo, L., and Oliva, R. (2011). COCOMAPS: a web application to analyze and visualize contacts at the interface of biomolecular complexes. Bioinformatics 27, 2915-2916. https://doi.org/10.1093/bioinformatics/btr484.
- 35. Holmgren, J., Bourgeois, L., Carlin, N., Clements, J., Gustafsson, B., Lundaren, A., Nygren, E., Tobias, J., Walker, R., and Svennerholm, A.M. (2013). Development and preclinical evaluation of safety and immunogenicity of an oral ETEC vaccine containing inactivated E. coli bacteria overexpressing colonization factors CFA/I, CS3, CS5 and CS6 combined with a hybrid LT/CT B subunit antigen, administered al. Vaccine 31, 2457-2464. https://doi.org/10.1016/j.vaccine.2013.03.027.
- 36. Liu, Y., Maciel, M., Jr., O'Dowd, A., Poole, S.T., Rollenhagen, J.E., Etobayeva, I.V., and Savarino, S.J. (2021). Development and comparison of a panel of modified cs17 fimbrial tip adhesin proteins as components for an adhesin-based vaccine against enterotoxigenic escherichia coli. Microorganisms 9, 1646. https://doi.org/10.3390/microorganisms9081646.
- 37. Zheng, W., Andersson, M., Mortezaei, N., Bullitt, E., and Egelman, E. (2019). Cryo-EM structure of the CFA/I pilus rod. IUCrJ 6, 815-821. https://doi.org/10.1107/S2052252519007966.
- 38. Pfab, J., Phan, N.M., and Si, D. (2021). DeepTracer for fast de novo cryo-EM protein structure modeling and special studies on CoV-related complexes. Proc. Natl. Acad. Sci. USA 118. https://doi.org/10.1073/pnas. 2017525118.
- 39. Krivov, G.G., Shapovalov, M.V., and Dunbrack, R.L. (2009). Improved prediction of protein side-chain conformations with SCWRL4. Proteins 77, 778-795. https://doi.org/10.1002/prot.22488.
- 40. Suloway, C., Pulokas, J., Fellmann, D., Cheng, A., Guerra, F., Quispe, J., Stagg, S., Potter, C.S., and Carragher, B. (2005). Automated molecular





- microscopy: the new Leginon system. J. Struct. Biol. 151, 41-60. https:// doi.org/10.1016/j.jsb.2005.03.010.
- 41. Pettersen, E.F., Goddard, T.D., Huang, C.C., Couch, G.S., Greenblatt, D.M., Meng, E.C., and Ferrin, T.E. (2004). UCSF Chimera A visualization system for exploratory research and analysis. J. Comput. Chem. 25, 1605-1612. https://doi.org/10.1002/jcc.20084.
- 42. Liebschner, D., Afonine, P.V., Baker, M.L., Bunkóczi, G., Chen, V.B., Croll, T.I., Hintze, B., Hung, L.W., Jain, S., et al. (2019). Macromolecular structure determination using X-rays, neutrons and electrons: recent developments in Phenix. Acta Crystallogr. D Struct. Biol. 75, 861-877. https://doi. org/10.1107/S2059798319011471.
- 43. Croll, T.I. (2018). ISOLDE: a physically realistic environment for model building into low-resolution electron-density maps. Acta Crystallogr. D Struct. Biol. 74, 519-530. https://doi.org/10.1107/S2059798318002425.
- 44. Emsley, P., Lohkamp, B., Scott, W.G., and Cowtan, K. (2010). Features and development of coot. Acta Crystallogr. D Biol. Crystallogr. 66. 486-501. https://doi.org/10.1107/S0907444910007493.
- 45. Case, D.A., Aktulga, H.M., Belfon, K., Ben-Shalom, I.Y., Brozell, S.R., Cerutti, D.S., Cheatham, T.E., III, Cisneros, G.A., Cruzeiro, V.W.D., Darden, T.A., et al. (2021). Amber. https://ambermd.org.
- 46. Waterhouse, A., Bertoni, M., Bienert, S., Studer, G., Tauriello, G., Gumienny, R., Heer, F.T., de Beer, T.A.P., Rempfer, C., et al. (2018). SWISS-MODEL: homology modelling of protein structures and complexes. Nucleic Acids Res. 46, W296-W303. https://doi.org/10.1093/ nar/akv427.

- 47. Fällman, E., Schedin, S., Jass, J., Andersson, M., Uhlin, B.E., and Axner, O. (2004). Optical tweezers based force measurement system for quantitating binding interactions; system design and application for the study of bacterial adhesion. Biosens. Bioelectron. 19, 1429-1437. http:// linkinghub.elsevier.com/retrieve/pii/S0956566303004615.
- 48. Andersson, M., Czerwinski, F., and Oddershede, L.B. (2011). Optimizing active and passive calibration of optical tweezers. J. Opt. 13, 044020. https://doi.org/10.1088/2040-8978/13/4/044020.
- 49. Andersson, M., Fällman E., Uhlin, B.E., and Axner, O. (2006). Technique for determination of the number of PapA units in an E. Coli P pilus. Proc. SPIE 6088, Imaging, Manipulation, and Analysis of Biomolecules, Cells. and Tissues IV, 608814. https://doi.org/10.1117/12.642261.
- 50. Maier, J.A., Martinez, C., Kasavajhala, K., Wickstrom, L., Hauser, K.E., and Simmerling, C. (2015). ff14SB: improving the accuracy of protein side chain and backbone parameters from ff99SB. J. Chem. Theory Comput. 11, 3696-3713. https://doi.org/10.1021/acs.jctc.5b00255.
- 51. Jorgensen, W.L., Chandrasekhar, J., Madura, J.D., Impey, R.W., and Klein, M.L. (1983). Comparison of simple potential functions for simulating liquid water. J. Chem. Phys. 79, 926-935. https://doi.org/10.1063/1. 445869
- 52. Joung, I.S., and Cheatham, T.E. (2008). Determination of alkali and halide monovalent ion parameters for use in explicitly solvated biomolecular simulations. J. Phys. Chem. B 112, 9020-9041. https://doi.org/10.1021/ ip8001614.

Article



STAR***METHODS**

KEY RESOURCES TABLE

REAGENT or RESOURCE	SOURCE	IDENTIFIER	
Bacterial and virus strains			
Escherichia coli strain BL21-Al(pMAM2), expresses CFA/I pili	Naval Medical Research Center, Silver Spring, MD	BL21-AI(pMAM2)	
Escherichia coli strain LSN 03-016011/A (O8:H,LT,CS17), expresses CS17 pili	Naval Medical Research Center, Silver Spring, MD	LSN 03-016011/A (O8:H,LT,CS17)	
Escherichia coli strain 7179A-2(pRA101), expresses CS20 pili	Naval Medical Research Center, Silver Spring, MD	7179A-2(pRA101)	
Chemicals, peptides, and recombinant proteins			
octyl β-D-glucopyranoside	Dojindo	Catalog #0001 CAS 29836-26-8	
Histatin-5 peptide	21st Century Biochemicals	DSHAKRHHGYKRKFHEKHHSHRGY	
Deposited data			
EM images and resulting density map, CFA/I pili	This paper	EMDB: EMD-28150	
CFA/I pili structure	This paper	PDB: 8EHR	
EM images and resulting density map, CS17 pili	This paper	EMDB: EMD-28151	
CS17 pili structure	This paper	PDB: 8EHS	
EM images and resulting density map, CS20 pili	This paper	EMDB: EMD-28152	
CS20 pili structure	This paper	PDB: 8EHT	
CFA/I pili structure – lower resolution	Zheng et al., 2019 ³⁷	PDB: 6NRV	
P pili structure	Hospenthal et al., 2017 ³³	PDB: 5FLU	
Type 1 pili structure	N/A	PDB: 6Y7S	
Software and algorithms			
RELION 3.1.1	Zivanov et al., 2018 ²⁰	www3.mrc-lmb.cam.ac.uk	
DeepTracer	Pfab et al., 2021 ³⁸	deeptracer.uw.edu	
SCWRL4	Krivov et al., 2009 ³⁹	dunbrack.fccc.edu/lab/scwrl	
Leginon	Suloway et al., 2005 ⁴⁰	emg.nysbc.org/redmine/projects/leginon	
SerialEM	Mastronarde, 2005	bio3d.colorado.edu/SerialEM/; www.nexperion.net/serialem	
Chimera	Pettersen et al., 2004 ⁴¹	www.cgl.ucsf.edu/chimera	
ChimeraX	Pettersen et al., 2021	www.cgl.ucsf.edu/chimerax	
Phenix	Liebschner et al., 2019 ⁴²	phenix-online.org/	
ISOLDE	Croll, 2018 ⁴³	isolde.cimr.cam.ac.uk	
Coot	Emsley et al., 2010 ⁴⁴	www2.mrc-lmb.cam.ac.uk/personal/ pemsley/coot/	
Amber20/Amber Tools 21	Case et al., 2021 ⁴⁵	ambermd.org	
Swiss MODELLER	Waterhouse et al., 2018 ⁴⁶	swissmodel.expasy.org	
VMD	Humphrey et al., 1996 ³²	www.ks.uiuc.edu/Research/vmd/	
LabView	National Instruments	www.ni.com	
MatLab R2020b	MathWorks	www.mathworks.com	
Origin 2021	OriginLab Corporation	www.originlab.com	
Other			
UltrAuFoil gold grids	Quantifoil	R1.2/1.3, 300 mesh	
FEI TF20 Electron Microscope	FEI (now ThermoFisher Scientific)	TF20	
ThermoFisher Scientific Titan Krios Electron Microscope	ThermoFisher Scientific	Titan Krios	
Gatan K3 Direct Electron Detector	Gatan	K3 Summit	
Optical Trap Setup	Magnus Andersson, Pl. Umeå University	Dahlberg et al., 2022 ⁹	





RESOURCE AVAILABILITY

Lead contact

Further information and requests for resources and reagents should be directed to and will be fulfilled by the lead contact, Esther Bullitt (bullitt@bu.edu).

Materials availablity

This study did not generate new unique reagents.

Data and code availability

- Cryo-EM data have been deposited at the EMDB and are publicly available as of the date of publication. Accession numbers are listed in the key resources table.
- Protein model data have been deposited at the PDB and are publicly available as of the date of publication. PDB identification numbers are listed in the key resources table.
- Any additional information required to reanalyze the data reported in this paper is available from the lead contact upon request.
- This paper does not report original code.

EXPERIMENTAL MODEL AND SUBJECT DETAILS

- CFA/I pili were expressed on Escherichia coli strain BL21-Al(pMAM2) bacteria and CS17 pili were expressed on Escherichia coli strain LSN 03-016011/A (O8:H,LT,CS17). Bacteria were grown on Luria-Bertani agar plates with 50 mg/mL kanamycin at 37°C without (CFA/I) or with (CS!7) the addition of 1.5q bile salt/liter for 24 h, pelleted and resuspended in 10mM Tris, 75mM NaCl (pH 7.4). Sample was heated to 65°C for 25 min to extract the pili, and cells were removed by centrifugation at 10,000xg. To precipitate CFA/I pili, 4M NaCl was added to a final concentration of 300mM; 0.5M MgCl 2 was added to a final concentration of 0.1 M, stirred overnight at 4C, and centrifuged at 25,000xg for 40 min. Pili were resuspended in 10mM Tris, pH 7.4 and addition of MgCl 2 was repeated two more times. Final pellet was resuspended in and dialyzed against the buffer.
- CS20 pili were expressed on Escherichia coli strain WS7179A-2/pRA101. Bacteria were grown on Luria-Bertani agar plates with 50 mg/mL kanamycin at 37°C for 24 h, pelleted and resuspended in PBS. Sample was heated to 65°C for 25 min to extract the pili, and cells were removed by centrifugation at 10,000xg. To precipitate CS20 pili, 0.24 g/mL ammonium sulfate was added to the supernatant at 4C, overnight. Pili were pelleted by centrifugation at 12,000xg and resuspended in PBS. Precipitation and pelleting were repeated. Pili were resuspended in 10mM MOPS, pH 7 and dialyzed against this buffer.
- Bacterial strains used to express pili are listed in the key resources table, and belong to the Naval Medical Research Center.

METHOD DETAILS

Sample preparation for cryo-EM

The concentrations of each filament were optimized in order to maximize the number of individual filaments per image while minimizing the amount of overlap between them. The surfactant and spreading agent, octyl β -D-glucopyranoside, was added at 12 nM to each protein sample directly before it was added to the grid. The following concentrations were used for grid freezing: 2 mg/mL of CFA/I, 1.5 mg/mL of CS17 and 1.8 mg/mL of CS20. For the CFA/I sample, we also added the 24 amino acid-long peptide, Histatin-5 at a concentration of 4 μM to our grid in an attempt to visualize the peptide bound to CFA/I. As noted in our later methods section, despite further processing, no density was found. After adding the surfactant, 1.5 µL of the protein solution was applied to a freshly glow discharged holey, UltrAuFoil R1.2/1.3 300 mesh grid (Quantifoil, Jena, Germany), blotted for 6 s, and immediately plunge-frozen in liquid ethane using a Vitrobot Mark III system (FEI/ThermoFisher Scientific, Hillsboro, OR).

Cryo-EM data collection and processing

Freezing conditions were optimized using images from an FEI TF20 cryo-EM, and data for analysis were collected on a Titan Krios transmission electron microscope operated at 300 kV (Thermo Fisher Scientific, Hillsboro, OR) at the Purdue Cryo-EM Facility (West Lafayette, IN). Movies were collected on a Gatan K3 Summit direct electron detector (Gatan/AMETEK, Berwyn, PA) using Leginon⁴⁰ at a nominal magnification of 81,000 x corresponding to a pixel size of 0.539 Å using a 20 eV energy filter with a dose rate of 17.21 e $^-$ /Å 2 /s, for a total exposure of 3.12 s and an accumulated dose of 53.70 e $^-$ /Å 2 . Frames were recorded every 0.08 s for a total of 40 frames per movie, with 4,809 movies collected for CFA/I pili, 4,921 movies for CS17 pili, and 5,236 movies for CS20 pili.

For all three filaments, image reconstructions were carried out using Relion 3.1.1. Movies were motion-corrected using MotionCor2 with pixels binned 2x, for a final pixel size of 1.078 Å. After motion correction, the contrast transfer function (CTF) was estimated using CtfFind 4.1.13. Initially, filaments from \sim 200 micrographs were manually selected and extracted as overlapping segments. Segment lengths were 216, 213, and 220 Å, for CFA/I, CS17, and CS20.

Structure Article



We then performed 2D classification and 2D averaging on the manually picked particles to create templates for autopicking. After autopicking produced 6,094,726 segments of CFA/I; 5,358,559 of CS17; and 9,590,890 of CS20, we performed 2D classification in order to remove false positives, ice contaminated, and damaged specimen images from the autopicked images. We further curated our three datasets by performing 2D classification, resulting in 2,411,300, 2,447,711, and 3,352,944 particles (CFA/I, CS17, CS20), followed by a single round of 3D classification into 8 classes using a RELION tau parameter of 14. For these classifications, we imposed the approximate helical symmetry of each filament, which had been defined from previous literature³⁷ or a subset of manually picked filaments. The initial symmetry values used were a rise of 8.6 Å and twist of 113.3° for CFA/I, rise of 8.8 Å and twist of 108° for CS17, and a rise of 8.9 Å and twist of 112.3° for CS20. After 25 iterations of classification, we picked the segments from the best single class (reported resolutions of ~ 4.5 Å) to continue to RELION auto-refine, resulting in final datasets that contained 325,069 segments of CFA/I, 231,783 segments of CS17, and 381,251 segments of CS20.

The first refinements were performed using featureless cylinders as a reference, while subsequent refinements utilized the previous refinement, low-pass filtered to 30 \mathring{A} , as a reference. Once the first reconstruction was performed, subsequent refinements used a solvent mask for each filament, created in RELION, that masked the central 50 % of the segment. This increased the reconstruction resolution by focusing the refinement on the center of the filament to reduce effects from filaments that were not perfectly straight and to reduce noise from the solvent. In addition, during these refinements, we performed helical symmetry searches to refine the symmetries. These symmetries converged in subsequent refinements.

Following the mask creation from our initial refinement, we then ran two iterations of CTF refinement and Bayesian polishing, after which no improvement in resolution or reconstruction quality was seen. The resolutions of the three maps were calculated using the gold standard FSC _{0.143}. The final resolution for CFA/I was 3.2 Å, CS17 was 3.3 Å, and CS20 had a final resolution of 3.4 Å.

In addition to this analysis, which allowed us to visualize the filaments with extraordinary detail, we also tried to resolve the 24 amino acid-long peptide added to the CFA/I sample. However, after exhaustive 3D classification efforts and attempts at single-particle analysis, no density associated with the peptide was located. For this reason, we expect that the peptide was not bound to the filaments used for reconstruction, as the backbone of our 3.2 Å CFA/I structure matched with our previous 4.3 Å resolution structure.

Model building for the filaments

CFA/I

To model the CFA/I subunit, CfaB, into our reconstruction, we used the previously published structure of CFA/I (PDB:6NRV). Initially, we extracted a single subunit from the 6NRV PDB file and fit it into the centrally located subunit within our reconstruction. Since our reconstruction possessed much higher resolution features, we observed that portions of the subunit fell outside of our density. In order to initially reposition the backbone and side-chains into our new reconstruction, we performed a single real-space refinement in PHENIX with five macrocycles of global minimization, rigid body fitting of the full complex, and local grid search using secondary structure and Ramachandran restraints. This produced a subunit that fit well into our density.

Following the refinement of a single subunit, we created a larger filament by fitting multiple copies of the refined subunit into the reconstruction using the UCSF Chimera fit-in-map command. Once a full filament was built, we manually refined the centrally located subunit in ISOLDE to reduce clashes and ensure proper map-to-model fit, ⁴³ extracted the centrally located subunit and again rebuilt the filament model using the Chimera fit-in-map tool. This ensured that each subunit within the filament was refined with other subunits adjacent to it, as without this, the subunits on the edge of our model could be modelled into 'unoccupied' density, producing unrealistic models. After creating our final filament reconstruction, we validated the model using phenix.validation_cryoem⁴² and all relevant statistics were compiled into the cryo-EM data collection, refinement and validation tables.

CS17

By comparing our CS17 and CFA/I cryo-EM reconstructions, it became clear that there was significant structural similarity. Fitting the CFA/I model into the CS17 map using the Chimera fit-in-map tool revealed that the backbones were nearly superimposable. Based on this observation, we created an initial CS17 homology model of CsbA from CfaB using the SWISS_MODELLER suite of programs⁴⁶ After producing a homology model of a single subunit, we placed it into our cryo-EM density using the fit-in-map command. The backbone fit well within the reconstruction, and two additional C-terminus amino acid residues not present in CfaB, K144 and T145, were added manually in coot.⁴⁴ After this process, we began refining the structure.

To refine the filament, multiple copies of our homology model were fit into the CS17 reconstruction to create a filament model, using the CFA/I filament as a template. After, we performed real-space refinement in PHENIX with five macrocycles of global minimization, rigid body fitting of the full complex, and local grid search using secondary structure and Ramachandran restraints. This created a model that fit well to the density, but still had a high clash score. To address this, we further manually refined the centrally located subunit in ISOLDE. After minimizing the clashscore, the central subunit was extracted from the structure file and multiple copies were refit into the cryo-EM density using the Chimera fit-in-map tool. After refitting the model, we performed validation using phenix.validation_cryoem and all relevant statistics were compiled into the cryo-EM data collection, refinement and validation tables.

CS20

There were no published structures of CS20 and no atomic models of pilins with high enough genetic similarity to produce a homology model. We therefore used the *de novo* structure prediction program DeepTracer, ³⁸ using only the CsbA amino acid sequence and our 3.4 Å reconstruction density map to model the backbone of the subunit5. Following the pipeline described in the original DeepTracer paper, after the backbone prediction we used the program, SCWRL4, ³⁹ to predict the side-chain orientations. Using





this workflow, we obtained a full model for the CS20 subunit fitted into our cryo-EM density. Although the backbone largely fit well into the density, further refinements maximized the model's fit to the map density and reduced atom clashes.

Subsequent refinements of the CS20 filament were very similar to the CS17 and CFA/I workflows. Initially, we fit multiple copies of the de novo model into the cryo-EM density to create a filament pdb to be passed through real-space refinement in PHENIX with five macrocycles of global minimization, rigid body fitting of the full complex, and local grid search using secondary structure and Ramachandran restraints. After this refinement, we manually refined the centrally located subunit in ISOLDE to further maximize fit to map as well as minimize clashes. Once complete, the central subunit was extracted from the pdb and multiple copies were used to rebuild the filament model using the Chimera fit-in-map tool. After fitting the subunits into the filament, we performed validation using phenix.validation_cryoem and all relevant statistics were compiled into the cryo-EM data collection, refinement and validation tables

Interaction energy and buried surface area calculations

Interaction energies were used to determine the strength of association between individual subunits within the pili filaments. We performed this analysis to determine the strength of the interactions that must break in order for an individual subunit to begin to unwind from the filament. These interactions primarily include the n to n+3 and to the residues from n+4 that sit in the n+3 groove in CFA/1, CS17, and type 1 pili. However, for CS20 and P pili the staple also plays a role. Interaction energies were calculated using the NAMD protocol in VMD³² and they include both electrostatic and van der Waals interactions. Buried surface areas were calculated using COCOMAPS. 34 Values were computed for interactions between n and n+3 and n+4 subunits for all pilus types.

Filament unwinding using optical tweezers

To measure the biophysical properties of CS17 pili, we used a custom-made force-measuring optical tweezer set-up constructed around an inverted Olympus IX71 microscope (Olympus) equipped with a water-immersion objective (UPlanSApo60xWIR, x60/ 1.2 NA; Olympus) and a 1,920x1,440 pixel CMOS camera (C11440-10C, Hamamatsu). The system design has been described previously.⁴⁷ To sample force data with a high signal-to-noise ratio with a minimal amount of drift, we used the Allan variance method to identify noise. 48 We used the power spectrum method to calibrate the trap by sampling the microsphere's position at 131,072 Hz and averaging 32 consecutive datasets acquired for 0.25 s each. 25 To extend a pilus, we moved the piezo stage at a constant speed of 100 nm/s and sampled the force and position at 50 Hz.

In a DFS measurement a pilus that underwent constant unwinding in region II was extended for a preset distance (~ 3 μm) with velocities above the steady-state velocity.²⁶ Prior to DFS measurement a pilus was extended at steady-state velocity (0.1 μm/s) to identify the total length of the unwinding region as well as to reduce multi-pilus bindings to a single pilus binding to the bead. With a known length of region II, a pilus was partially rewound to provide a 3-um-long region for unwinding without reaching region III. The 3 μm region was then extended at five different velocities: 0.1, 0.4, 1.6, 6.4, and 25.6 μm/s. The corresponding force and position responses were acquired at 5 kHz sampling rate. After each pull a pilus was allowed to rewind to the start position under steady-state velocity (0.1 μm/s), and the stage was paused for 2 s before the next pull was initiated with higher velocity.

Description of the sticky-chain model

The sticky-chain model is an analytical model that describes the force-extension response of a helixlike pilus under tensile stress.²⁴ The model is built upon elastic elongation of tandem connected subunits and rate equations for force-assisted bond-opening according to Bells theory. 30 In the model, a bond can either be in a closed state A or an open state B, and the bond opening rate of region II under an applied force, F, is given as a rate equation according to,

$$dN_B / dt = k_{AB}^{th} e^{F\Delta x_{AT}/kT} - k_{AB}^{th} e^{(\Delta V_{AB} - F\Delta x_{TB})/kT},$$
 (Equation 1)

where k is the Boltzmann factor, T the temperature, k_{AB}^{th} is the thermal bond opening rate, Δx_{AT} and Δx_{TB} are the bond lengths, i.e., the distance from the closed and open state to the transition barrier, and ΔV_{AB} is the energy difference between the two states. For high extension velocities, the refolding rate in Equation 1 (second term on the right side) can be neglected, and the rate equation simplifies to an expression relating the unwinding force to the extension velocity, \dot{L} , as

$$F(\dot{L}) = kT / \Delta x_{AT} \ln(\dot{L} / \dot{L}^{th}),$$
 (Equation 2)

where Lith the thermal extension speed. 49 By using Equation 2 it is thereby possible to use unwinding force data at different velocities to assess the bond length, Δx_{AT} . Further, from the data, it is also possible to find the corner velocity, that is the transition point that separates the steady-state and dynamic region. Thus, the corner velocity can be defined as the maximum extension velocity of a pilus before any increase in velocity leads to an increased unwinding force.

Molecular dynamics simulations

All molecular dynamics simulations and system preparation were performed using the software Amber20/AmberTools21.45 The ff14SB force field⁵⁰ was used for protein parameters, and the TIP3P force field⁵¹ was used for water molecules. The Joung and Cheatham parameters were used for monovalent ions. 52 All modeled systems were comprised of seven pilin subunits (a 7mer system), in addition to the complementary β-strand in the base subunit of each 7mer filament to complete the pilin fold. The structures used for each of the systems are listed in the Supporting Information. Each system was energy minimized, heated, and equilibrated

Structure Article



using the same protocol before steered molecular dynamics simulations were carried out. Steered molecular dynamics simulations were carried out at a constant pulling speed of 1 Å/ns, and five trial runs were carried out for each system. Contacts are defined as alpha carbons of two amino acids coming within a 0.8 nm cutoff of one another.

The Amber20/AmberTools21⁴⁵ program was used to parameterize and simulate all of the systems. Each system consisted of a 7mer filament, along with a complementary β-strand inserted into the base subunit to complete its pilin fold. The initial coordinates used for each system were: (1) CFA/I (PDB: 8EHR), (2) CS17 (PDB: 8EHS), (3) CS20 (8EHT), (4) P pilus (PDB: 5FLU)⁸, and (5) Type 1 pilus (PDB: 6Y7S). Systems were oriented such that the filament axis points along the z-direction, which was also the direction of pulling in the steered molecular dynamics simulations. The force fields used to describe the interactions in the system included the FF14SB force field⁵⁰ for protein parameters and the TIP3P force field⁵¹ for the description of water. Counterions were parameterized using the Joung and Cheatham monovalent ion parameter set. 52 All systems were placed into a rectangular box of TIP3P water, and the box was constructed to include 12 Å of water in the x and y directions and 160 Å of water in the z direction. The large buffer in the z direction allowed for large-scale unwinding of the 7mer filament under force. The CS20, P pilus, and Type 1 pilus also contain disulfide bonds, and those were created using tLeap during system parameterization by changing cysteine amino acids names from CYS to CYX in the input PDB coordinate files.

Preparation of each of the systems for steered molecular dynamics simulations followed the approach previously used to prepare the P pilus system. Here we describe the main features of this protocol, as well as some of the specifics for the CFA/I, CS17, CS20, and Type 1 pili. The P pilus simulation data presented in this paper is derived from the simulations conducted in 9 and therefore the specific details of the P pilus methodology are not described again here, as they are found in that publication.

For all systems, energy minimization was carried out using a total of 5000 cycles (first 3000 steepest descent minimization steps followed by 2000 conjugate gradient minimization steps). During minimization a force constant of 10.0 kcal mol $^{-1}$ Å $^{-2}$ was applied to all alpha carbons in the system, while all other atoms remained unrestrained. After minimization was completed, all systems were gradually heated to the target temperature of 300 K. The first stage of heating was carried out at constant volume and lasted 50 ps. During that stage the systems were heated from 0 K to 100 K over 20 ps, and then the system was maintained at 100 K for an additional 30 ps. Next, a constant pressure phase of heating was used, during which the system temperature was gradually increased from 100 K to the final target temperature of 300 K. The same force constant of 10.0 kcal mol $^{-1}$ Å $^{-2}$ was applied to all alpha carbons in the system during the heating phase to maintain overall protein structure. The next stage of simulation was an equilibration in the NPT ensemble. During equilibration the temperature was held at 300 K and the pressure was set to 1 bar. The restraints on the alpha carbons of the filament systems were gradually changed over time during equilibration as described in Table S1.

For all steered molecular dynamics simulations, the jar = 1 option was used in Amber20. Steered molecular dynamics simulations were performed using the same temperature and pressure conditions as in equilibration described above. The collective variable for pulling on the system was defined as the z-component of the center of mass distance between the alpha carbons of subunit 1 (the tip subunit) and the alpha carbons of subunits 5, 6 and 7 (not including the alpha carbons of the N-terminal extension (NTE) β -strand of subunit 5 to allow for its flexibility during extension, and not including the alpha carbons of the NTE β-strand inserted into subunit 7 that completes its pilin fold). The tip subunit is defined as the "pulled" group and the second selection at the base of the filament is referred to as the "fixed" group. We apply a force constant of 0.5 kcal mol $^{-1}$ Å $^{-2}$ to restrain the alpha carbons in the fixed group. More detailed descriptions of the amino acids used to define the fixed and pulled groups of atoms are given below. Restraining the fixed group of atoms allows us to unwind four of the subunits in the 7mer system while the bottom three subunits remain fixed in space representing the bottom of the filament bound to a surface. The additional restraints also serve the purpose of overall rotational and translational motion of the 7mer system while the steered molecular dynamics simulations are carried out. Systems were extended at a constant speed of 1 Å/ns, and the pulling force was applied along the z-direction which coincides with the filament axis.

The pulling spring used a spring stiffness of 10 kcal mol $^{-1}$ Å $^{-2}$. All stages of the simulations, including heating, equilibration, and steered molecular dynamics, used a 2 fs time step which was possible due to the application of the SHAKE algorithm. Constant temperature was maintained using the Langevin thermostat with a 1 ps⁻¹ collision frequency, and the Monte Carlo barostat was used to keep a constant pressure of 1 bar. The particle mesh Ewald method was used for calculations of the long range electrostatic forces and otherwise the cutoff for real space interactions was set to 8 A.

Definitions of restrained selections during stages 6 and 7 of equilibration, and definitions of fixed and pulled groups during steered molecular dynamics simulations:

CFA/I

- Equilibration stage 6.
 - restraints on alpha carbons of residues 1–13 (NTE β-strand of base subunit 7), residues 1–146 of subunit 7, residues 1–146 of subunit 6, and residues 16-146 of subunit 5.
- Equilibration stage 7.
 - restraints on alpha carbons of residues 1-13 (NTE βstrand of base subunit 7), residues 1-146 of subunit 7, residues 1-146 of subunit 6, residues 16-146 of subunit 5, and residues 1-146 of subunit 1.
- Steered molecular dynamics.
 - restraints on alpha carbons of residues 1–13 (NTE βstrand of base subunit 7), residues 1–146 of subunit 7, residues 1–146 of subunit 6, and residues 16-146 of subunit 5.





- Pulled group defined as the alpha carbons of residues 14–146 of subunit 1.
- fixed group defined as the alpha carbons of residues 1-13 (NTE β-strand of base subunit 7), residues 1-146 of subunit 7, residues 1-146 of subunit 6, and residues 16-146 of subunit 5.

CS17

- Equilibration stage 6.
 - restraints on alpha carbons of residues 1–12 (NTE β-strand of base subunit 7), residues 1–145 of subunit 7, residues 1–145 of subunit 6, and residues 16-145 of subunit 5.
- Equilibration stage 7.
 - restraints on alpha carbons of residues 1–12 (NTE β-strand of base subunit 7), residues 1–145 of subunit 7, residues 1–145 of subunit 6, residues 16–145 of subunit 5, and residues 1–145 of subunit 1.
- Steered molecular dynamics.
 - restraints on alpha carbons of residues 1–12 (NTE β-strand of base subunit 7), residues 1–145 of subunit 7, residues 1–145 of subunit 6, and residues 16-145 of subunit 5
 - Pulled group defined as the alpha carbons of residues 16–145 of subunit 1.
 - Fixed group defined as the alpha carbons of residues 1–12 (NTE β-strand of base subunit 7), residues 1–145 of subunit 7, residues 1-145 of subunit 6, and residues 16-145 of subunit 5.

CS20

- Equilibration stage 6.
 - restraints on alpha carbons of residues 1–19 (NTE β-strand of base subunit 7), residues 1–172 of subunit 7, residues 1–172 of subunit 6, and residues 24-172 of subunit 5.
- Equilibration stage 7.
 - restraints on alpha carbons of residues 1–19 (NTE β-strand of base subunit 7), residues 1–172 of subunit 7, residues 1–172 of subunit 6, residues 24-172 of subunit 5, and residues 1-172 of subunit 1.
- Steered molecular dynamics.
 - restraints on alpha carbons of residues 1–19 (NTE β-strand of base subunit 7), residues 1–172 of subunit 7, residues 1–172 of subunit 6, and residues 24-172 of subunit 5
 - Pulled group defined as the alpha carbons of residues 22–172 of subunit 1.
 - Fixed group defined as the alpha carbons of residues 1–19 (NTE β-strand of base subunit 7), residues 1–172 of subunit 7, residues 1-172 of subunit 6, and residues 24-172 of subunit 5.

P pilus

- Equilibration stage 6.
 - restraints on alpha carbons of residues 1–20 (NTE β-strand of base subunit 7), residues 1–163 of subunit 7, residues 1–163 of subunit 6, and residues 21-163 of subunit 5.
- Equilibration stage 7.
 - restraints on alpha carbons of residues 1–20 (NTE β-strand of base subunit 7), residues 1–163 of subunit 7, residues 1–163 of subunit 6, residues 21–163 of subunit 5, and residues 1–163 of subunit 1.
- Steered molecular dynamics.
 - restraints on alpha carbons of residues 1–20 (NTE β-strand of base subunit 7), residues 1–163 of subunit 7, residues 1–163 of subunit 6, and residues 21-163 of subunit 5.
 - Pulled group defined as the alpha carbons of residues 16–163 of subunit 1.
 - Fixed group defined as alpha carbons of residues 1–20 (NTE β-strand of base subunit 7), residues 1–163 of subunit 7, residues 1-163 of subunit 6, and residues 21-163 of subunit 5

Type 1 pilus

- Equilibration stage 6.
 - restraints on alpha carbons of residues 1–18 (NTE β-strand of base subunit 7), residues 1–159 of subunit 7, residues 1–159 of subunit 6, and residues 20-159 of subunit 5.
- Equilibration stage 7.
 - restraints on alpha carbons of residues 1–18 (NTE β-strand of base subunit 7), residues 1–159 of subunit 7, residues 1–159 of subunit 6, residues 20-159 of subunit 5, and residues 1-159 of subunit 1.
- Steered molecular dynamics.
 - restraints on alpha carbons of residues 1–18 (NTE β-strand of base subunit 7), residues 1–159 of subunit 7, residues 1–159 of subunit 6, and residues 20-159 of subunit 5.
 - Pulled group defined as the alpha carbons of residues 21–159 of subunit 1.
 - Fixed group defined as alpha carbons of residues 1–18 (NTE β-strand of base subunit 7), residues 1–159 of subunit 7, residues 1-159 of subunit 6, and residues 20-159 of subunit 5.

Structure

Article



QUANTIFICATION AND STATISTICAL ANALYSIS

- Fourier shell correlations were calculated using RELION; see Figure S2.
- PDB models were validated using PDB software; available at the PDB.
- Force extension data (n = 40) and dynamic force extension data (n = 13) were analyzed using Matlab 2021 and corresponding figures were made in Origin 2021.
- The correlation analysis was made in Origin 2021.
- Steered molecular dynamics runs: n = 5 for each pilus.